

Mass assembly and AGN activity at $z \gtrsim 1.5$ in the dense environment of XDCPJ0044.0-2033

M. Lepore^{1,2}, A. Bongiorno², P. Tozzi¹, A. Travascio³, L. Zappacosta², E. Merlin², and R. Fassbender⁴

¹ INAF-Osservatorio Astronomico di Arcetri, Largo Enrico Fermi 5, 50125, Florence, Italy.
e-mail: marika.lepore@inaf.it

² INAF-Osservatorio Astronomico di Roma, Via di Frascati 33, 00078, Monteporzio Catone, Rome, Italy.

³ Università degli Studi di Milano Bicocca, Piazza dell'Ateneo Nuovo 1, 20126, Milan, Italy.

⁴ Max Planck Institut für extraterrestrische Physik, Giessenbachstrasse 1, 85748 Garching, Germany.

November 9, 2022

ABSTRACT

Context. XDCPJ0044.0-2033 is the most massive galaxy cluster known at $z > 1.5$ and its core shows a high density of galaxies which are experiencing mergers and hosting nuclear activity.

Aims. We present a multi-wavelength study of a region of $24 \text{ kpc} \times 24 \text{ kpc}$ located $\sim 157 \text{ kpc}$ from the center of the cluster, for which we have photometric and spectroscopic observations. Our main goal is to investigate the environmental effects acting on the galaxies inhabiting this high density region.

Methods. We performed sources identification and photometric analysis on high-resolution Hubble Space Telescope (HST) images in F105W-, F140W- and F160W-band and spectroscopic analysis of the Near-Infrared (NIR) KMOS data in H and YJ bands. In addition, we analyzed the deep *Chandra* ACIS-S X-ray exposure.

Results. We find that the analyzed region hosts at least 9 different sources, 6 of them confirmed to be cluster members within a narrow redshift range $1.5728 < z < 1.5762$, and therefore is denser than the very central, more massive region of the cluster previously analyzed by [Travascio et al. \(2020\)](#). These sources form two different complexes (Complex M and Complex N) at a projected distance of $\sim 13 \text{ kpc}$, which are undergoing merging on an estimated timescale of 10-30 Myr. One of the sources shows the presence of a broad $H\alpha$ emission line and is classified as Type-1 Active Galactic Nucleus (AGN). This AGN is associated to an X-ray point-like source, whose emission appears moderately obscured (with intrinsic absorption $N_H \sim 10^{22} \text{ cm}^{-2}$) and hosts a relatively massive black hole (BH) with mass $M_{BH} \sim 10^7 M_\odot$, which is accreting with an Eddington ratio of ~ 0.2 .

Conclusions. We conclude that the analyzed region is consistent with being the formation site of a secondary Brightest Cluster Galaxy (BCG). These findings, together with an in-depth analysis of the X-ray morphology of the cluster, suggest a merging scenario for the entire cluster, with two massive halos both harboring two rapidly evolving BCGs on the verge of being assembled. Our results are also consistent with the scenario in which the AGN phase in member galaxies is triggered by gas-rich mergers, playing a relevant role in the formation of the red sequence of elliptical galaxies observed in the center of local galaxy clusters.

Key words. XDCPJ0044.0-2033 Galaxies: active Galaxies: clusters: individual Galaxy: evolution Galaxies: interactions Galaxies: high-redshift Galaxy: formation Galaxies: star formation Galaxies: kinematics and dynamics

1. Introduction

The standard Λ CDM cosmological model predicts a hierarchical scenario for the formation and evolution of large scale structures in an expanding Universe ([Bond et al. 1991](#)). In this scenario, the first structures in the Universe are halos of Dark Matter (DM) that, through merging, form increasingly massive halos. The baryonic matter then falls into the potential wells of these DM halos and, through gas accretion and/or merging, forms stars and galaxies ([White & Rees 1978](#)).

Eventually, the environment in which a galaxy is located influences its evolution. In particular, this evolution depends on the presence of cold molecular gas and, in dense environments, processes as galaxy-galaxy mergers ([Aarseth & Fall 1980](#); [Park & Hwang 2009](#)), harassment ([Moore et al. 1996](#)), strangulation ([Balogh et al. 2000](#); [van den Bosch et al. 2008](#)) and ram-pressure stripping ([Gunn & Gott J. Richard 1972](#); [McCarthy et al. 2008](#)) can occur and affect the transportation of the cold gas thus accelerating the evolution of a galaxy.

Galaxy clusters are the ideal laboratories for studying the effects

of dense environments on the evolution of galaxies and their properties, especially in their early phases when gas-rich, rapidly forming galaxies strongly interact with each other. In this framework, the study of galaxy clusters at different redshift is key to understand the role of the environment in the evolution/transition from star forming (SFGs) to red and passive galaxies ([Alberts et al. 2016](#)).

On one hand, in the local Universe and up to $z \sim 1.4$, the dense cores of galaxy clusters are preferentially populated by massive early-type galaxies that form a tight sequence in the color-magnitude diagram (CMD), the so called Red Sequence ([Bell et al. 2004](#)). Among them, the BCG, typically a giant elliptical, stands out for its high luminosity ($M_V \sim -23$) and stellar mass ($M \sim 10^{12} M_\odot$). While at $z < 1.4$ the SFGs are preferentially located in the cluster outskirts, where the local galaxy density is low, a reversal of the star formation (SF)-density relation starts to appear at $z \gtrsim 1.4$. Therefore, massive, high-redshift galaxy clusters host more SFGs in their core ([Brodwin et al. 2013](#)), forming the so called Blue Sequence ([Bell et al. 2004](#)), and may not show the presence of a BCG. This inversion sug-

gests that the galaxy cluster populations undergo one or more processes able to affect the SF activity in a relatively short time.

Also the AGN activity in clusters shows a similar trend compared to the SFGs. As an example, [Alberts et al. \(2016\)](#), studying SF and AGN activity in 11 galaxy clusters at $1 < z < 1.75$, suggested a co-evolution between SF and AGN driven by merger activity. The current framework, in agreement with semi analytic models and simulations, predicts a scenario in which galaxy major mergers induce starburst and also fuel BH accretion, triggering an AGN phase ([Hopkins et al. 2006](#)). Later, the feedback phase of AGNs, in form of winds and outflows, lead to SF quenching and to the formation of passive elliptical galaxies, as observed in clusters in the local Universe ([Narayanan et al. 2010](#)). However, it is not clear yet how these processes happen and how galaxy properties can be influenced by the presence of nuclear activity and vice versa. In this context, $z \sim 1.2$ is a crucial epoch to observe young galaxy clusters, where we do expect a high rate of mergers among galaxies and a higher rate of nuclear and SF activity.

Over the years, several large area surveys have been designed to reveal high redshift, massive ($M \gtrsim 10^{14} M_{\odot}$) galaxy clusters using optical/infrared/X-ray observations. Among them: SpARCS ([Wilson et al. 2006](#)) is based on the detection of distant clusters by means of their red galaxy population; SPT ([Williamson et al. 2011](#)) and ACT ([Menanteau et al. 2010](#)) are based on the Sunyaev-Zel'dovich effect (SZ); and the XMM-Newton Distant Cluster Project (XDCP, [Fassbender et al. 2011](#)) is based on the study of diffuse X-ray emission from the Intra-cluster Medium (ICM).

With these surveys it was possible to state that the SF-density relation gradually changes starting from $z > 1$, (e.g. [Hilton et al. 2010](#); [Fassbender et al. 2011](#); [Tadaki et al. 2012](#); [Fassbender et al. 2014](#); [Santos et al. 2014, 2015](#)). Also, a decline in SF in clusters over cosmic time ([Alberts et al. 2014](#)), paralleled by a decrease in black hole activity has been unambiguously observed and quantified. The fraction of AGNs falls by two orders of magnitude in clusters from $z \sim 1.5$ to $z \sim 0$ ([Galamez et al. 2009](#); [Martini et al. 2013](#)), with AGNs preferentially residing in the infall regions of clusters ([Pimbblet et al. 2013](#)). Quantifying, at the same time, the effects of cosmic evolution and the environmental effects is, therefore, a key aspect of the evolution of massive galaxies.

In this paper we focus on the high- z galaxy cluster XDCP J0044.0-2033 (or "Gioiello" cluster, hereafter XDCP0044; [Fassbender et al. 2011](#), [Santos et al. 2011](#)), the most massive cluster known at $z > 1.5$ (see Figure 1, *left panel*). It has been found thanks to its extended X-ray emission, discovered in the XDCP survey ([Fassbender et al. 2011](#)). Deep *Chandra* observations confirmed strong diffuse emission (with centroid coordinates $RA = 00 : 44 : 05.2$ and $DEC = -20 : 33 : 59.7$) typical of virialized clusters ([Tozzi et al. 2014](#)). XDCP0044 is thus in a quite advanced dynamical state and is an ideal laboratory to study the mass assembly at high- z , the interplay between galaxies, nuclear activity, and the intergalactic gas in dense environment.

Concerning the galaxy population, XDCP0044 shows a strong inversion of the SF-density relation. Indeed, [Santos et al. \(2014\)](#) found that the total SF rate within the projected core area ($r < 250$ kpc) is $SFR = 1875 \pm 158 M_{\odot}/yr$ (considering only the spectroscopic members), four times higher compared to the SFR in the cluster outskirts. In addition, X-ray point-like emission has been detected from at least 2 member galaxies within ~ 250 kpc from the cluster center (labeled as 3 and 5 in Figure 1, *left panel*). Two additional unresolved X-ray sources may turn out to be additional cluster members, but they do not have redshift

measurements yet. Furthermore, radio JVLA data show the presence of at least four sources emitting in the radio band and an extended radio emission associated to Complex A (see [Travascio et al. 2020](#)). In particular, the core region (~ 70 kpc \times 70 kpc) of XDCP0044, studied by [Travascio et al. \(2020\)](#), is the densest among those observed at $z > 1.5$ and shows the presence of two luminous, obscured and highly accreting AGNs and an optically obscured Type-2 AGN, with signatures of ongoing merging. Multiple AGN activity and high SF in the core of a high- z cluster suggest that these processes have a key role in shaping the nascent BCG observed at the center of local clusters.

On the basis of these results, we decided to investigate star formation and nuclear activity in another region located ~ 157 kpc from the core of XDCP0044, that appears to be extremely dense and active, as shown by the presence of an X-ray unresolved source at its center, the intense star formation at the level of $SFR = 825 \pm 120 M_{\odot}/yr$ (source ID 95 in [Santos et al. 2014](#)), and the presence of a compact radio source with luminosity $L_{1.5GHz} = 2.6 \pm 0.3 \times 10^{24} W/Hz$ (source r3 in [Travascio et al. 2020](#)). To perform our study, we use high-resolution HST photometric data combined with K-band multi-object spectrometer at ESO VLT (KMOS IFU) observations and X-ray *Chandra* data. Figure 1 shows the HST RGB (F105W+F140W+F160W) image of XDCP0044 with overlaid the soft ([0.5-2.0] keV) band X-ray contours of the extended emission and the 5 X-ray point-like sources detected by [Tozzi et al. \(2014\)](#).

The paper is organized as follows. In Section 2 we describe the analyzed data while in Section 3 we present the source identification and photometric analysis, along with spectroscopic and kinematic analysis. In Section 4 we present the detailed analysis of the X-ray AGN. We discuss our findings in Section 5, and finally summarize our conclusions in Section 6.

2. Observation and Data Reduction

HST images: HST images of XDCP0044 have been obtained in 2015 with the Wide Field Camera 3 (WFC3) in F105W, F140W, F160W and F814W bands (Program: 13677, PI: S. Perlmutter) with the following exposure times: 4689 sec in F105W, 5189 sec in F140W, 2595 sec in F160W and 1620 sec in F814W. In our analysis, we use the images obtained by combining the archival drizzled (DRZ) frames, after performing the astrometry and aligning them. Due to the low S/N, the F814W band has not been included (see also [Travascio et al. 2020](#)). The depth of the three images at 5σ is [28.53, 28.33, 28.18] respectively for F105W, F140W and F160W.

KMOS IFU data: observations in YJ (spectral coverage: 1.0251.344 μm) and H (spectral coverage: 1.4561.846 μm) bands have been obtained in 2013 (Program ID: 092.A0114(A), PI: R. Fassbender). Here we analyzed the KMOS data centered on the X-ray source 3 ($RA=0:44:05.4570$; $DEC=-20:34:16.672$) with a $2.8'' \times 2.8''$ field of view (see the magenta square in Figure 1 *right panel*), for a total target integration time of $\sim 4.4h$ in YJ band and $\sim 1.25h$ in H band. At the redshift of the cluster (i.e. $z \sim 1.6$), YJ-band samples the [OIII] and $H\beta$ emission lines with a resolving power $R=3600$ while H-band samples the $H\alpha$ region with $R=4000$. The data have been reduced using the pipeline with the Software Package for Astronomical Reduction with KMOS (SPARK; [Davies et al. 2013](#)), which includes dark correction, flat fielding, illumination correction, wavelength calibration and sky subtraction ([Davies et al. 2011](#)). The data are then combined according to the spatial shift of the objects in each frame.

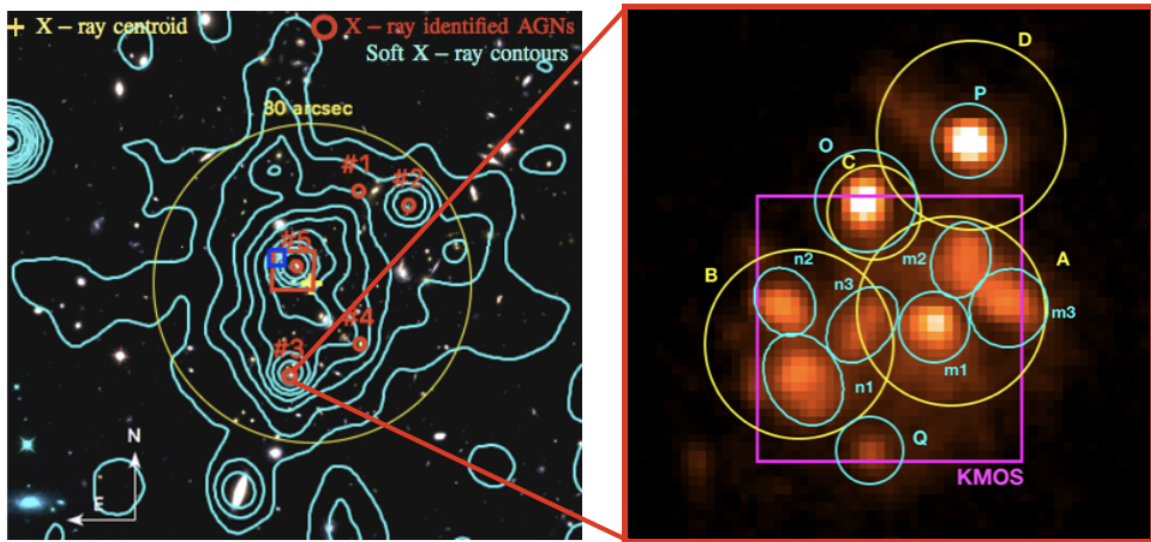


Fig. 1. *Left Panel*, adapted from Travascio et al. 2020: HST RGB (F105W+F104W+F160W) image of XDCPJ0044 with overlaid the soft ([0.5-2] keV) bands X-ray contours. The yellow circle is centered on the X-ray extended emission centroid (yellow cross, RA=00:44:05.2 and DEC=-20:33:59.8) and has a radius of 30 arcsec, corresponding to ~ 250 kpc. The red circles mark the 5 X-ray point-like sources detected by Tozzi et al. (2014). *Right Panel*: HST image in F105W band. The yellow circles mark the sources detected in ground based HAWK-I J and Ks bands by Fassbender et al. (2014) while cyan circles mark the sources detected in HST. The magenta square is the KMOS field of view.

Chandra X-ray data: the data used for the X-ray spectral analysis are obtained from six different observations performed in September, October and November 2013 (PI: P. Tozzi) with the ACIS-S instrument of the *Chandra* observatory for 370 ks of exposure time. We consider X-ray data in the energy range 0.3-7.0 keV, where *Chandra* ACIS detector is most sensitive and well calibrated. Details on observations and data reduction can be found in Tozzi et al. (2014).

3. Data Analysis

3.1. NIR source identification and photometry

We focus our photometric analysis on the $24 \text{ kpc} \times 24 \text{ kpc}$ region observed by HST (see *right panel* of Figure 1). Ground based (HAWK-I J and Ks bands and Subaru/Suprime V and i bands) photometric analysis in this region has been already performed by Fassbender et al. (2014) and Santos et al. (2014) who identified 3 different sources, i.e. A, C and D in Figure 1 (*right panel*), in addition to the previously discovered spectroscopic member B (Santos et al. 2011).

Thanks to the higher resolution, HST images allow us to distinguish more sources compared to ground based images. We used SExtractor (Bertin & Arnouts 1996) to detect and deblend the sources, identifying a total of 9 objects. As shown in Figure 1 *right panel*, A and B sources identified with HAWK-I consist of three different objects, i.e. $m1+m2+m3$ and $n1+n2+n3$, respectively. Moreover, an additional faint source (Q) has been detected only in HST data.

The photometric analysis has been performed using λ -PHOT (Merlin et al. 2019). We tried to estimate the flux contamination from neighboring sources by taking two different photometric measurements. Photometric values are first obtained within elliptical apertures defined by eye to include most of the visible light coming from each galaxy (APER), which is then converted in magnitudes in the F105W, F140W and F160W bands using

as zero points $zp = 26.2, 26.4$ and 25.9 , respectively¹. A second photometric measurement is obtained simply considering the fluxes assigned to each galaxy in the segmentation map created by SExtractor (ISO). We consider the difference between the two measurements as a reasonable approximation of the contamination between sources. Final uncertainties are computed as the combination of the statistical error provided by λ -PHOT and the contamination uncertainty. We find that, given the extremely crowded region, the final errors are dominated by contamination. The derived HST F105W-, F140W- and F160W-band AB system magnitudes, together with the associated errors, and the HST coordinates (RA and DEC) are reported in Table 1.

3.2. NIR spectroscopy

Here we present the spectroscopic analysis of the sources identified in HST. Spectra in YJ- and H-band have been extracted on the position of the sources identified in HST, using a fixed aperture of 3 pixel (i.e. $0.6''$) in diameter on the KMOS data cubes. In the H-band spectrum of 6 out of the 9 sources we found individual emission lines with SNR ranging from ~ 3 to ~ 10 . As these sources belong to a crowded region, it is reasonable to assume they are physically close to each other, i.e. having similar redshift. Moreover, since these complexes are within a galaxy cluster, we can guess that the redshift of the galaxies is approximately similar to the average cluster redshift. Thus, we assume that these lines represent $H\alpha$ transitions, which is also one of the strongest line expected. For two of them ($m1$ and $n1$), an $H\beta$ 4861\AA line is also observed in the YJ-band spectrum, although we found these lines into a noisy region contaminated by the sky lines. A zoom-in of the spectral region showing the $H\alpha$ line for these sources is shown in Figure 2, while the redshifts derived by fitting the observed lines are listed in Table 2 together with the FWHM of the line and the SNR calculated as the ratio between the signal at the peak of the narrow $H\alpha$ emis-

¹ See http://www.stsci.edu/hst/wfc3/ir_phot_zpt.

Table 1. Identified sources in the high resolution HST images (see Figure 1, *right panel*).

HST ID	RA	DEC	m_{F105W}	m_{F140W}	m_{F160W}
m1	0:44:05.4570	-20:34:16.672	23.54±1.32	22.61±1.06	22.17±0.92
m2	0:44:05.4369	-20:34:15.962	23.91±0.06	23.38±0.01	23.13±0.01
m3	0:44:05.4008	-20:34:16.470	23.75±0.01	23.06±0.13	22.81±0.17
n1	0:44:05.5556	-20:34:17.221	23.54±0.44	23.35±0.54	23.24±0.57
n2	0:44:05.5694	-20:34:16.404	24.09±0.46	23.99±0.61	23.88±0.67
n3	0:44:05.5178	-20:34:16.551	24.31±0.39	23.91±0.56	23.69±0.63
O	0:44:05.5080	-20:34:15.348	23.08±0.37	22.37±0.32	22.21±0.32
P	0:44:05.4300	-20:34:14.715	23.12±0.36	22.55±0.37	22.45±0.39
Q	0:44:05.5050	-20:34:17.968	24.75±1.14	24.19±1.05	24.06±1.09

Notes. Columns are: HST ID and position (RA and DEC), F105W-, F140W- and F160W-band magnitudes with their uncertainties including the statistical error computed by λ -PHOT and the contamination uncertainty.

sion line and the σ of the signal in the spectrum where there is only the continuum.

Redshifts range from $z = 1.5728$ to $z = 1.5762$ and, given the small dispersion ($\Delta z = 0.0034$), all 6 galaxies are therefore spectroscopically confirmed cluster members. Given the redshifts of the sources and their apparent position, we can identify in the system two subgroups: **Complex M**, which includes m1, m2 and m3 whose redshifts range from $z = 1.5756$ to $z = 1.5762$ ($\Delta z = 0.0006$) and **Complex N**, consisting of n1, n2 and n3 with z between 1.5728 and 1.5732 ($\Delta z = 0.0004$). Note that the redshift of source n3 is tentative given the low Signal-to-Noise Ratio (SNR) of the line. Interestingly, the analysis of the spectrum of source m1 shows that the $H\alpha$ emission line is broad ($FWHM > 1500$ km/s, see Figure 2 m1-panel). Source m1 is therefore classified as a broad line AGN (BLAGN, see Section 4 for more details). Finally, from the analysis of the YJ-band spectra, an $H\beta\lambda 4861\text{\AA}$ line is observed for sources m1 and n1, confirming their redshift (see Figure 3).

For all 6 galaxies for which a redshift has been measured, we have estimated the rest-frame luminosity at 5100\AA ($L_{5100\text{\AA}}$) and the V-band absolute magnitude from the flux measured at the wavelength of interest, by interpolating the HST photometric points in F105W and F140W bands. These values are listed in Table 2.

3.3. Kinematic analysis of the super complex of galaxies

XDCP0044 shows a complex dynamical state. One hint of this particular state is the presence of diffuse emission between galaxies. Therefore, we search for emission lines at the same redshift of the analyzed system. Particularly, the IFU data allow us to perform a spatially resolved study of the kinematics of the $H\alpha$ emission line.

As a first step, we create a velocity shift map of the narrow $H\alpha$ emission line relative to source m1 to identify patterns of gas and galaxies. We choose source m1 because it is an AGN (see Section 4), therefore, is the best candidate to be the most massive galaxy and the gravitational center of the system. We estimated the velocity shifts for each galaxy considering source m1 as reference and following the relation by Harrison (1974):

$$v_{shift} = \left(\frac{\lambda_{obs} - \lambda_{cen}}{\lambda_{cen}} \right) c, \quad (1)$$

where λ_{obs} is the observed wavelength of the narrow $H\alpha$ emission line in a given source, while λ_{cen} is the wavelength corresponding to the $H\alpha$ emission line of source m1. Figure 4 shows a map in which different colors indicate the velocity shift of each

source with respect to source m1. This map has been obtained extracting the total emission of narrow and broad $H\alpha$ emission lines for each source considering the regions used for photometric analysis (see Section 3.1). We then studied the dynamics of the diffuse emission by looking at the narrow $H\alpha$ emission line pixel by pixel, excluding the broad $H\alpha$ emission line (see Figure 5). The SNR cut of these map is ~ 2.5 .

A visual inspection of the maps clearly confirm that sources m1, m2 and m3 belong to the same complex of galaxies (**Complex M**), while sources n1, n2 and n3 to **Complex N**, with a negative velocity shift (~ 300 km/s) with respect to the **Complex M**. Given the small velocity difference, **Complex M** and **Complex N** are expected to merge individually to form two more massive galaxies. Eventually, **Complex M** and **Complex N** may also merge with each other, finally forming a second BCG, as anticipated by the analysis of Fassbender et al. (2014). These results will be further discussed in Section 5.1.

Then, we focus on a region located south of source m1, where we identify diffuse emission at the same wavelength of the narrow $H\alpha$ emission line of m1, which is also visible in the HST IR images. In addition, we find diffuse emission also between sources m1 and n3, with a very high velocity shift (~ 450 km/s), although the detection has a low significance. Both detections can be interpreted as diffuse gas in the midst of galaxies, destabilized by recent galaxy-galaxy encounters. In the case of the $H\alpha$ emission below source m1, this could also be interpreted as extended (~ 7 kpc) Narrow Line Region (ENLR) around source m1 (see e.g. Hippelein et al. 1996, Husemann et al. 2019). We will not discuss further the diffuse emission, arguing that deeper IR integral field spectroscopy may reveal in greater detail the dynamics of the diffuse baryons in the dense cluster core, helping in tracing the complex dynamical interaction occurring during the merging phase.

4. Analysis of the source m1

4.1. X-ray spectroscopy of m1

As discussed in Section 3.2, the source m1 is identified as a BLAGN and has been detected as a point-like source in the *Chandra* image by Tozzi et al. (2014). Here we present a detailed spectral analysis of the *Chandra* data of m1. The source+background spectrum has been extracted from a circular region of radius ~ 1 arcsec centered on source m1, within which we measure $72.8^{+9.6}_{-8.5}$ net counts in the 0.3–7 keV band. The background spectrum (rescaled by the extraction area and subtracted to the source+background spectrum) has been extracted from an annular region of inner and outer radii 4 and 10 arcsec, respec-

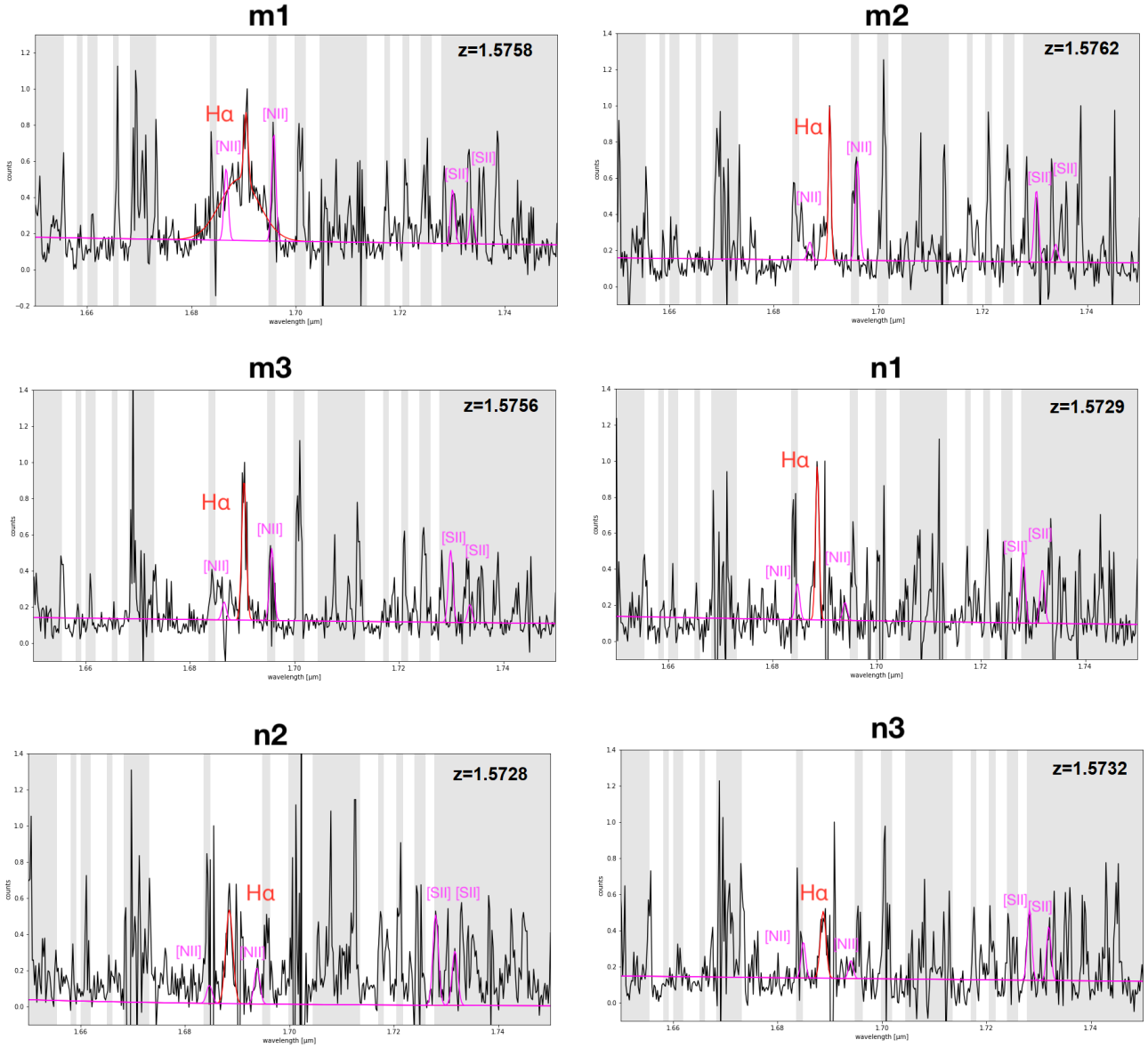


Fig. 2. Zoom-in of the H-band spectra around the $H\alpha$ line of the 6 confirmed cluster members. In red it is shown the power-law+gaussian fit of the emission line, while the magenta line is used to mark the continuum and the [NII] and [SII] emission lines. The derived spectral properties are listed in Table 2.

tively. The data from these six observations (see Section 2) are combined to form a single spectrum using the FTOOLS script `addascaspec`. Then, the spectra are binned so that there was at least 1 count per bin and modeled using the software XSPEC v. 12.12.0 in the [0.3-7.0 keV] band. Also, we performed the analysis using Cash statistics (Cash 1979). The rebinned spectrum is shown in Figure 6.

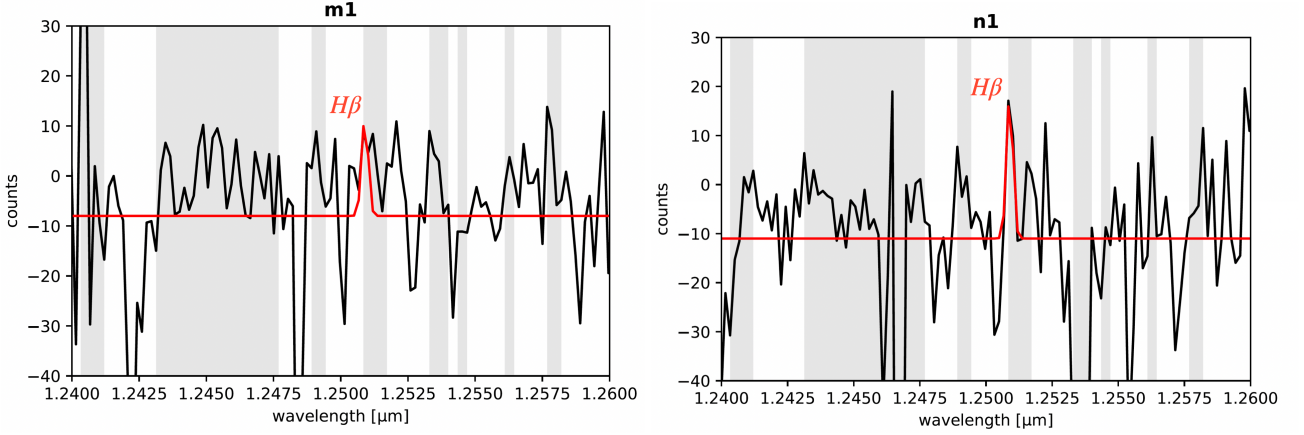
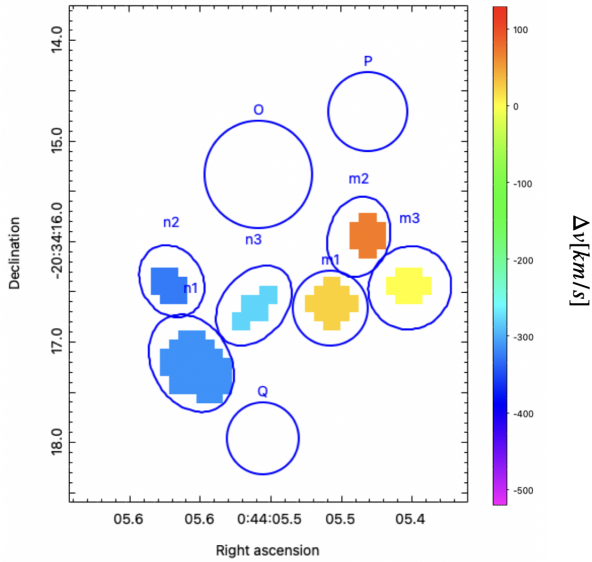
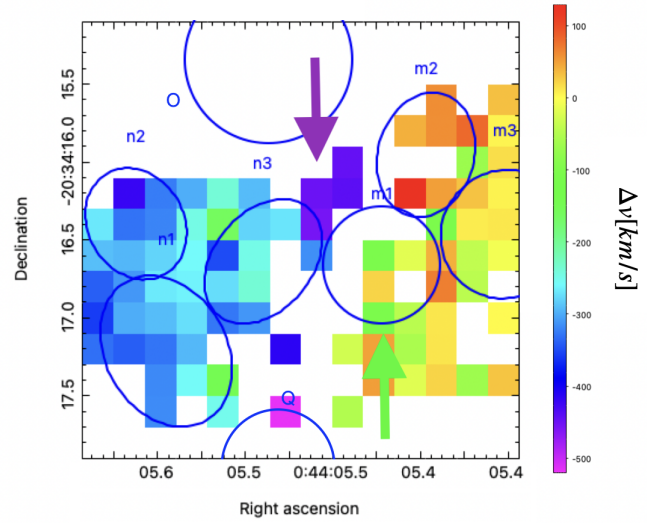
To fit the spectrum we used a model that includes three terms: a power law which models the emission related to the Comptonization of photons from the hot electron corona surrounding the accretion disk, a term which accounts for the Galactic absorption and a term for the intrinsic absorption. The results show that the photon index Γ is between 1.8 and 2.0, the typical value for Type1 AGNs, and that the source is moderately obscured ($\text{Log}[N_{\text{H}}/\text{cm}^2] = 22.4^{+0.2}_{-0.5}$), assuming a Galactic column density fixed at $\text{Log}[N_{\text{H}}/\text{cm}^2] = 20.1$ (HI4PI Collaboration

et al. 2016). The X-ray properties of the source m1 are reported in Table 3. From the derived values, and assuming a redshift of 1.5758 (see Section 3.2), the intrinsic, unabsorbed luminosity is measured to be $\text{Log}[L^{\text{X}}_{[2-10\text{keV}]}] = 43.4^{+0.3}_{-0.4}$ in the [2-10 keV] rest-frame band. These results are consistent within 1σ with those found in Tozzi et al. (2014), where an aperture of 1.5 arcsec is used for the extraction of the spectrum.

In order to test possible variability in flux, slope and absorption during the three months period of observations, we considered the three spectra separately obtained by merging the corresponding Obsid in three different periods, and jointly modeled them. In this case, the model used to fit the spectra is the same as in the case of a single spectrum with the addition of a constant that takes into account possible changes in the source flux. We find that the signal in each temporal bin is too low to search for

Table 2. Results of the KMOS spectral analysis.

ID	z	FWHM _B km/s	Log(L _{HαB}) erg/s	FWHM _N km/s	Log(L _{5100Å}) erg/s	M _V	SNR
m1	1.5758	1551±102	~42.84	167±30	43.85±0.21	-22.39±0.09	3.88
m2	1.5762			177±19	43.41±0.67	-21.17±0.32	6.14
m3	1.5756			177±14	43.58±0.59	-21.64±0.28	8.24
n1	1.5729			177±12	43.47±0.73	-21.22±0.35	9.85
n2	1.5728			226±27	43.32±0.33	-20.82±0.16	4.95
n3	1.5732*			176±42	43.23±0.36	-20.67±0.16	2.79

Notes. (1) source ID; (2) redshift; (3) FWHM of the H α emission line (broadB component); (4) Luminosity of the broad H α emission line; (5) FWHM of the H α emission line (narrowN component); (6) 5100Å Luminosity; (7) Vband absolute magnitude; (8) SNR ratio.

Fig. 3. Zoom-in of the YJ-band spectra around the H β line respectively for source m1 and n1.

Fig. 4. Velocity shift map of the individual sources, with respect to m1. Blue circles mark the sources detected in HST .

Fig. 5. Velocity shift map of the narrow H α emission line. Green and purple arrows mark the H α extended emission detected outside the main sources.

4.2. Bolometric luminosity, BH mass, and Eddington ratio

From the 5100Å luminosity, we derived the bolometric luminosity using the relation

$$K_{5100\text{\AA}} = \frac{L_{\text{bol}}}{L_{5100\text{\AA}}} \quad (2)$$

spectral variability, while, focusing on the flux normalization, we found no hints for variability.

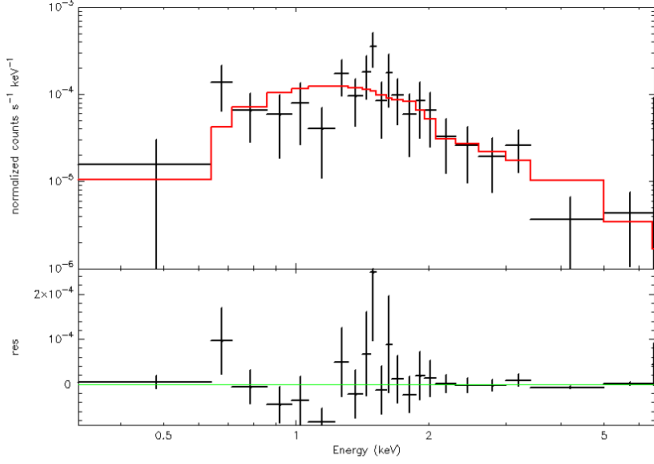


Fig. 6. *Chandra* X-ray spectrum of m1 with the best-fit model (red line). Lower panel shows the residuals.

where $K_{5100\text{\AA}}$ is the bolometric correction given by Krawczyk et al. (2013) (see also Saccheo et al. 2022). Considering $K_{5100\text{\AA}} = 4.33 \pm 1.29$, the value obtained for source m1 is $\text{Log}[L_{\text{bol}}/\text{erg/s}] = 44.49^{+0.11}_{-0.15}$.

It is also possible to compute the bolometric luminosity using the X-ray luminosity at [2-10 keV] band and assuming the bolometric corrections by Duras et al. (2020):

$$K_X(\text{Bol}) = \frac{L_{\text{bol}}}{L_X} = a \left[1 + \left(\frac{\log(L_{\text{bol}}/L_{\odot})}{b} \right)^c \right] \quad (3)$$

with $a = 12.76 \pm 0.13$, $b = 12.15 \pm 0.01$ and $c = 18.78 \pm 0.14$ as in Table 1 of Duras et al. (2020) for Type1 AGN. The value obtained for source m1 is $\text{Log}[L_{\text{bol}}^X/\text{erg/s}] \sim 44.52$, in agreement to the one obtained from the 5100Å luminosity above. Given the nuclear origin of the AGN X-ray emission, such agreement ensures us that the 5100Å luminosity is not contaminated by the host galaxy.

We then estimated the BH mass of m1 using the virial formula applied to the Broad Line Regions (BLRs). In particular, since in the spectrum of m1 we detected a broad $H\alpha$ emission line, we used the relation found by Greene & Ho (2005) which relates to the FWHM and the luminosity of the broad $H\alpha$ emission line according to the relation:

$$M_{\text{BH}} = 2.0^{+0.4}_{-0.3} \times 10^6 \left(\frac{L_{H\alpha}}{10^{42}\text{erg/s}} \right)^{0.55 \pm 0.02} \left(\frac{\text{FWHM}_{H\alpha}}{10^3\text{km/s}} \right)^{2.06 \pm 0.06} M_{\odot}. \quad (4)$$

Using the values of $\text{FWHM}_{H\alpha}$ and $L_{H\alpha}$ from Table 2, we derived the mass of the central BH which is $\text{Log}[M_{\text{BH}}/M_{\odot}] = 7.15 \pm 0.32$. As a further check, we computed the BH mass using, together with the FWHM of the broad $H\alpha$ emission line, the absorption corrected [2-10 keV] X-ray luminosity as in Eq. (4) of Bongiorno et al. (2014):

$$\log M_{\text{BH}} = 7.11 + 2.06 \log \frac{\text{FWHM}_{H\alpha}}{10^3\text{km/s}} + 0.693 \log \frac{L_{[2-10\text{keV}]}}{10^{44}\text{erg/s}}. \quad (5)$$

The obtained value is $\text{Log}[M_{\text{BH}}/M_{\odot}] = 7.08^{+0.40}_{-0.45}$, consistent with the value found above.

The error associated to the BH masses are given by the sum of

the statistical and systematic uncertainties. The systematic uncertainty in the $\text{Log}M_{\text{BH}}$ determination has been estimated in 0.3 dex to account for the observed scatter in the virial relation itself, while in the computation of the statistical errors, we take into account the errors in the 5100Å and X-ray luminosity, and the one on the FWHM measurement (in quadrature).

Furthermore, from the central BH mass it is possible to calculate the Eddington luminosity which is linked only to the mass of the body that is accreting according to the relation

$$L_{\text{Edd}} = 1.33 \times 10^{38} \left(\frac{M}{M_{\odot}} \right) [\text{erg/s}]. \quad (6)$$

Assuming $\text{Log}[M_{\text{BH}}/M_{\odot}] = 7.15 \pm 0.32$ ($7.08^{+0.40}_{-0.45}$), the Eddington luminosity of source m1 is $\text{Log}[L_{\text{Edd}}/\text{erg/s}] = 45.28 \pm 0.32$ ($45.21^{+0.40}_{-0.45}$).

Finally, we calculated the Eddington ratio

$$\lambda_{\text{Edd}} = \frac{L_{\text{bol}}}{L_{\text{Edd}}} \quad (7)$$

which describes the rate at which the central supermassive (SM) BH is accreting. We obtain a value in the range $\lambda_{\text{Edd}} \sim 0.17\text{--}0.20$. Therefore, we conclude that source m1 hosts a relatively small ($\sim 10^7 M_{\odot}$) and moderately accreting ($\lambda_{\text{Edd}} \sim 0.2$) SMBH. Its physical properties are summarized in Table 3.

5. Discussion

5.1. Mass assembly and time scales

Models and simulations (De Lucia & Blaizot 2007) predict that the mass of the galaxy population observed in clusters in the local Universe began to assemble at $z \sim 35$. At $z \sim 2.5$ the progenitors of massive galaxies start to form and at $z \sim 12$ merger activity reaches a peak. Then, the mass assembly proceeds through minor merging processes, leading to the formation of galaxies observed in the local Universe.

As we previously mentioned, $z \sim 1.6$ is a crucial epoch to study the mass assembly because it is close to the SF and BH activity peak (Madau & Dickinson 2014). The region of $24\text{ kpc} \times 24\text{ kpc}$ analyzed in this work includes a super complex formed by 6 up to 9 interacting galaxies, making it an extraordinarily dense region. The surface number density is measured to be $\sim 10^{-2}\text{ kpc}^{-2}$ in physical units. This can be seen as a lower limit, considering we find 9 sources identified in HST images. This region is denser than the core region of XDCPJ0044 (Travascio et al. 2020), which shows a surface number density one order of magnitude lower and also even denser than the core region of the Spiderweb protocluster at $z \sim 2.156$ (Roettgering et al. 1994, Pentericci et al. 1997, Miley et al. 2006), which shows a surface number density of $\sim 7 \times 10^{-4}\text{ kpc}^{-2}$ (Kuiper et al. 2011).

Furthermore, the 6 confirmed cluster members form two different complexes, Complex M and Complex N, which are located at a distance $d \sim 13\text{ kpc}$ and have a relative velocity $v \sim 300\text{--}400\text{ km/s}$. Simulations show that most pairs of galaxies near enough to each other, i.e. typically 20-30 kpc, and with a low velocity difference ($\sim 200\text{--}300\text{ km/s}$) will eventually merge on a short time scale (e.g. Patton et al. 2002, López-Sanjuan et al. 2011, López-Sanjuan et al. 2012). Indeed, the 6 to 9 interacting galaxies in the analyzed region will likely merge within a timescale comparable to dynamical friction (Conselice 2014).

It is also possible to estimate the collision timescale among sources in Complex M and sources in Complex N, considered pairs of galaxies in a dense environment. To estimate this

Table 3. Physical properties of the source m1.

ID	Log[L _{bol}] erg/s	Log[M _{BH}] M_{\odot}	λ_{Edd}	Log[L _X] erg/s	Log[N _H] cm^{-2}	Γ
m1	44.49 ^{+0.11} _{-0.15}	7.15 ± 0.32	~0.17-0.20	43.4 ^{+0.3} _{-0.4}	22.4 ^{+0.2} _{-0.5}	1.9 ^{+0.5} _{-0.4}

Notes. Log[L_{bol}] refers to the bolometric luminosity computed from $L_{[5100\text{\AA}]}$ with the bolometric correction by Krawczyk et al. (2013).

timescale we first computed the stellar mass of each galaxy resolved by HST images by performing SED-fitting procedure on HST photometry, HAWK-I J and Ks bands, Subaru/Suprime V and i bands. We used the Z-PHOT code (Fontana et al. 2000), with Bruzual & Charlot (2003) templates, Salpeter (1955) initial mass function and Calzetti et al. (2000) extinction. We adopted exponentially declining SF histories (τ models). However, for the detected sources n1, n2 and n3, the accuracy on photometry is not sufficient to constrain the SED, thus masses have been derived assuming different values of mass-to-light ratio, according to different population models (McGaugh & Schombert 2014). Mass values and associated uncertainties are listed in Table 4. Finally, we estimated the radius of the sources as the half-light radius obtained with SExtractor (Bertin & Arnouts 1996). The best-fitting masses of the sources in the analyzed region sum up to a total stellar mass of $\sim 10^{11} M_{\odot}$.

Then, we used the relation reported by Vijayaraghavan & Ricker (2013) to calculate the collision timescale:

$$t_{coll} = \frac{1}{n_{gal}\sigma_{cs}v_{gal}}, \quad (8)$$

where

- n_{gal} is the number density of galaxies in the analyzed region. In our case we considered the cluster members detected in the KMOS field of view in a sphere with radius of ~ 12 kpc (half of the KMOS field of view);
- σ_{cs} is the galaxy cross-section calculated as

$$\sigma_{cs} \sim \pi(r_1^2 + r_2^2) \left(1 + \frac{G(M_1 + M_2)}{(r_1 + r_2)v_{rel}^2} \right) \left(\frac{v_{esc}}{v_{gal}} \right)^{2/3}, \quad (9)$$

- with M_i and r_i are the mass and radius of the galaxy pair and v_{esc} the escape velocity from the system;
- v_{gal} is the velocity shift between the sources.

The resulting merging time is of the order of ~ 10 Myr for sources in Complex M and ~ 30 Myr for sources in Complex N. If we use the same approach to estimate the merging time between Complex M and Complex N we obtain an estimate of ~ 370 Myr for this two complexes to form a single source.

5.2. Nuclear and star formation activity

One of the results of this work is the presence of an AGN in a very dense ($\sim 4.9 \times 10^8 M_{\odot}/kpc^2$) and star-forming ($SFR=825 \pm 120 M_{\odot}/yr$, see Section 1) region at ~ 157 kpc from core of a galaxy cluster at $z > 1.5$. The properties of this AGN are relevant to the AGN-host galaxy co-evolution scenario. According to Martini et al. (2009), Albers et al. (2016), Bufanda et al. (2017) and other studies, the presence of an AGN in a galaxy cluster is directly correlated with the presence of gas-rich galaxies that, through merging, influence the transportation of molecular gas and consequently the AGN activity. The high SFR measured implies a large quantity of molecular gas surrounding the

system. The availability of this in-flowing gas means, in turn, that there are conditions for triggering BH accretion and, at the same time, sustain the vigorous SF itself. Clearly, the dense environment favour SFG mergers and thus again accelerate both SF and nuclear activity (Ellingson & Yee 1993).

The AGN at the center of the studied region appears to be moderately obscured ($\text{Log}[N_H/cm^2] \sim 22$), hosting a medium size ($M_{BH} \sim 10^7 M_{\odot}$) and moderately accreting ($\lambda_{Edd} \sim 0.2$) BH (see Section 4.1), providing a luminosity $\text{Log}[L_X/erg/s] \sim 43$. Following Sanders et al. (1988) and Hopkins et al. (2006) evolutionary models, this represents a specific phase in the AGN-galaxy co-evolution. In these models gas cools during galaxy mergers and fall onto the central BH, feeding its accretion and SF in the host galaxy. During this phase, the central BH is obscured by gas and dust. After all the gas is consumed or displaced by nuclear and stellar feedback, the AGN luminosity and star formation episodes decrease. Particularly, the AGN studied in this work may be in the early stages of accretion. During this phase we find a high SFR, due to the presence of cold gas, which is feeding also the central BH. According to this scenario, the AGN will continue to accrete gas from the environment/host galaxy, increasing its mass until, at some point, it will reach a critical mass and enter the feedback phase, beginning to emit winds and outflows. These winds and outflows eventually quench the SF in the host galaxy, driving it toward a red and passive galaxy, i.e. a possible second BCG located south of the cluster core.

5.3. XDCP0044: a double merging cluster

From the analysis of the surface brightness distribution of XDCP0044, Tozzi et al. (2014) found that this cluster shows the presence of two clumps (see Figure 7 left panel, magenta circles) with possibly different temperatures, the north clump with $kT = 7.1^{+1.3}_{-1.0}$ keV and the south clump with $kT = 5.5^{+1.2}_{-1.0}$ keV, which are consistent at slightly less than 2σ . To confirm the presence of two different clumps, we analyze the *Chandra* X-ray images with the *Sherpa* software in *ciao*.

We consider the AGN-subtracted *Chandra* X-ray image in the soft band and fit the data in this region with a double two-dimensional beta model plus background using Cash statistic, in order to find the emission peak of each clump. We find that the first peak is associated to the cluster core studied by Travaschio et al. (2020) (north clump), while the second peak is located south the cluster core, shifted with respect to the region studied in this work, as shown in Figure 7 (green and cyan cross, respectively, in the left panel). To better understand the results obtained from the analysis, we show the best-fit model and the residuals obtained with *Sherpa* in Figure 7 (central panel and right panel, respectively). We inspect the residuals and the SNR ratio map of the residuals to search for possible structure in the X-ray emission not accounted for by our double beta model. We do not find any significant residuals, expect for a weak hint of a slightly brighter arc in the overlapping region between the two

Table 4. Values of mass, with upper and lower limits, for the six sources in the KMOS field of view.

ID	$\text{Log}[M]$ M_{\odot}	$\text{Log}[M_{\text{Max}}]$ M_{\odot}	$\text{Log}[M_{\text{Min}}]$ M_{\odot}
m1	9.4	10.9	8.6
m2	10.1	10.3	8.8
m3	8.5	9.8	8.3
n1	9.4*	10.1*	8.9*
n2	9.2*	9.9*	8.8*
n3	9.2*	9.8*	8.8*

Notes. The values marked with "*" are those calculated assuming different mass-to-light ratios from [McGaugh & Schombert \(2014\)](#).

clumps. This shows that the two halo model is more than adequate to describe the data, and suggesting that further signs of the ongoing merger should be investigated with future, high resolution X-ray missions such as Lynx ([The Lynx Team 2018](#)) and AXIS ([Mushotzky & AXIS Team 2019](#); [Marchesi et al. 2020](#)).

To summarize, we note that the main halo (hosting the core studied by [Travascio et al. 2020](#)) is significantly brighter and can be considered virialized with an almost formed BCG at the center. Moreover, we note that the southern clump has a lower surface brightness, and that its X-ray centroid is far from Complex M and Complex N. However, the position of the X-ray centroid of the weaker halo may have been biased by the low signal. Finally, we note another feature consisting in a weak, but clearly visible extension toward the west, suggesting a very complex dynamical state that has not been modeled in the current analysis.

Despite our data set is not sufficient to provide a comprehensive explanation of the dynamical state of XDCPJ0044, we argue that we may be observing the merger of two halos, both recently virialized or in the process of being virialized, and each one with its own BCG in the assembling phase. We do expect that the two systems identified in this work, Complex M and Complex N, will merge within ~ 370 Myr to form a massive galaxy ($M_* \sim 10^{11} M_{\odot}$). Following the same procedure applied in Section 5.1, we suggest that these complexes will eventually join the massive galaxy formed by Complex A and Complex B in the core ([Travascio et al. 2020](#)) on a timescale of ~ 6 Gyr, which is in agreement with simulations ([Boylan-Kolchin et al. 2008](#); [Villalobos et al. 2013](#)).

6. Summary & Conclusions

Dense regions in high- z galaxy clusters are ideal laboratories to investigate the interplay between galaxies, nuclear activity and the intergalactic gas. In particular, we have analyzed high resolution multi-band HST images, NIR IFU KMOS spectroscopic data and the X-ray *Chandra* data of a small ($24 \text{ kpc} \times 24 \text{ kpc}$) but very dense region around one of the X-ray point-like sources discovered within the galaxy cluster XDCPJ0044 at $z \sim 1.6$, located $\sim 157 \text{ kpc}$ from its center. The main results of this paper can be summarized as follows:

1. thanks to the high resolution HST data, we found that the analyzed region is denser than expected from the analysis of ground based observations. In particular, up to 9 sources have been detected in only $24 \text{ kpc} \times 24 \text{ kpc}$. This is even denser than what found in the core of the cluster by [Travascio et al. \(2020\)](#) and in the core of the Spiderweb protocluster at $z \sim 2.156$. We have performed the photometric analysis of all the available HST bands, i.e. F105W, F140W and F160W, and computed the fluxes and magnitudes of the 9 identified
2. sources. These values have been then used to compute the monochromatic luminosities at 5100\AA .
3. From the KMOS IFU spectroscopic analysis, we found that at least 6 of the 9 sources detected in HST show a narrow $\text{H}\alpha$ emission line, and two of them also the $\text{H}\beta$ emission line. From the derived redshifts, which range from 1.5728 to 1.5762, we find that all 6 sources are confirmed cluster members. Moreover, the sources seems to be located in two different subgroups: Complex M and Complex N at a projected distance $d \sim 13 \text{ kpc}$. Complex M is formed by sources m1, m2 and m3, with redshift ranging from 1.5756 to 1.5762, and Complex N by sources n1, n2 and n3, with redshift ranging from 1.5728 to 1.5732.
4. IFU spectroscopic data allow us to study the kinematic of the analyzed complexes, through velocity shift maps of the narrow $\text{H}\alpha$ emission line. From such maps, we found that Complex N has a negative velocity shift ($\sim 300 \text{ km/s}$) with respect to Complex M. Moreover, from the velocity shift maps, we found significant emission below the source m1, at the same wavelength of the narrow $\text{H}\alpha$ emission line of m1, that can be interpreted either as a diffuse gas in the midst of galaxies, i.e. gas stripped during the merger, or as an ENLR around source m1. We also find hints of emission between the sources m1 and n3, with a high velocity shift ($\sim 450 \text{ km/s}$).
5. From the *Chandra* X-ray spectrum of source m1, we find a photon index between 1.8 and 2.0, typical of an AGN, and an obscuration of $N_H \sim 10^{22} \text{ cm}^{-2}$ for an intrinsic X-ray luminosity of $L_{[2-10]\text{keV}} \sim 10^{43} \text{ erg/s}$. We detected a broad $\text{H}\alpha$ emission line in the spectrum of source m1. This source is therefore classified as a BLAGN. By applying the virial formula, using the measured $\text{H}\alpha \text{ FWHM} > 1500 \text{ km/s}$ and luminosity, we estimate a SMBH mass of $M_{\text{BH}} \sim 10^7 M_{\odot}$.
6. The 5100\AA luminosity of the 6 confirmed cluster members have been derived by interpolating the computed HST fluxes at F105W and F140W. Source m1, with $\text{Log}[L_{5100\text{\AA}}/\text{erg/s}] \sim 43.85$, is the most powerful source, in agreement with the fact that it hosts an AGN. Moreover, by applying to m1 the AGN bolometric corrections by [Krawczyk et al. \(2013\)](#), we estimated the bolometric luminosity using $L_{5100\text{\AA}}$, finding $\text{Log}[L_{\text{bol}}/\text{erg/s}] \sim 44.49$. This value is in agreement with what found by applying the bolometric corrections by [Duras et al. \(2020\)](#) to the X-ray $[2-10]\text{keV}$ luminosity, confirming that the monochromatic luminosity at 5100\AA is related to a nuclear component.
7. Finally, from the BH mass and the bolometric luminosity, we derived the Eddington luminosity, $\text{Log}[L_{\text{Edd}}/\text{erg/s}] \sim 45.2$, and a relatively high Eddington ratio $\lambda_{\text{Edd}} \sim 0.2$.
8. While the merging time scale is estimated to be 10 Myr for Complex M and 30 Myr for Complex N, the two complexes, at a distance of $\sim 13 \text{ kpc}$ with a velocity shift of $\sim 300 \text{ km/s}$,

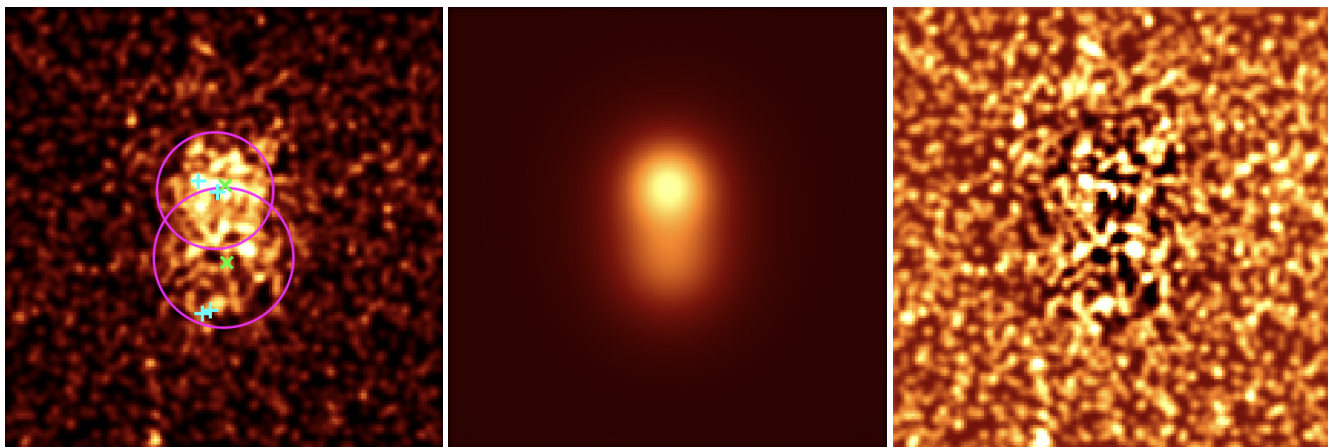


Fig. 7. *Left Panel:* AGN-subtracted *Chandra* X-ray image of XDCP0044. The magenta circles represent the north clump and south clump identified in Tozzi et al. (2014) with two different temperatures and the cyan crosses represent the four complexes identified in this cluster, Complex A and Complex B (Travascio et al. 2020) in the north and Complex M and Complex N in the south. The green crosses represent the X-ray emission peaks found with Sherpa image fitting. *Central Panel:* Best-fit model obtained with *Sherpa* of the AGN-subtracted X-ray image. *Right Panel:* Residuals obtained with *Sherpa*.

will likely merge within a timescale comparable to dynamical friction to form a massive galaxy, possibly the second BCG of XDCP0044.

8. After a revised analysis of the X-ray image of XDCP0044, we conclude that the two complex pairs (A+B, Travascio et al. (2020), and M+N) are most likely associated to two merging halos, with different properties in term of average ICM temperature and surface brightness.

To summarize, we investigated a region in the high-redshift galaxy cluster XDCP0044, suggesting that it is probably the formation site of one of the two BCGs of the cluster that is undergoing a major merger. These results corroborate a scenario in which AGN activity is triggered during the mergers between gas-rich galaxies which provide the fuel for both the AGN and the starburst activity. Given the high BH accretion rate and the high SF rate, the BH is expected to rapidly increase its mass during the galaxies' mergers and later, through feedback, quench the SF, leading to the formation of a massive and passive galaxy, as observed in local galaxy clusters. Deeper IR integral field spectroscopy may provide further insights into the dynamical state of the galaxy systems, and help in constraining their future evolution. As for the hot, diffuse baryons, the loss of sensitivity of the only arcsec resolution X-ray facility (*Chandra*) makes it impossible to go deeper in the X-ray band. However, high-resolution imaging of the SZ effect due to the ICM itself may be obtained thanks to ALMA. Also, thanks to the advent of JWST, detailed studies of the assembling galaxies in highz clusters will become more frequent, allowing us to reach a comprehensive description of a crucial phase in the formation and evolution of massive galaxies.

Acknowledgements. We thank G. De Lucia and E. Rasia for useful discussions, and the anonymous referee for the accurate comments on the paper.

References

- Aarseth, S. & Fall, S. 1980, *The Astrophysical Journal*, 236, 43
 Alberts, S., Pope, A., Brodwin, M., et al. 2014, *Monthly Notices of the Royal Astronomical Society*, 437, 437
 Alberts, S., Pope, A., Brodwin, M., et al. 2016, *The Astrophysical Journal*, 825, 72
 Balogh, M. L., Navarro, J. F., & Morris, S. L. 2000, *The Astrophysical Journal*, 540, 113
 Bell, E. F., Wolf, C., Meisenheimer, K., et al. 2004, *The Astrophysical Journal*, 608, 752
 Bertin, E. & Arnouts, S. 1996, *Astronomy and Astrophysics*, 117, 393
 Bond, J., Cole, S., Efstathiou, G., & Kaiser, N. 1991, *The Astrophysical Journal*, 379, 440
 Bongiorno, A., Maiolino, R., Brusa, M., et al. 2014, *Monthly Notices of the Royal Astronomical Society*, 443, 2077
 Boylan-Kolchin, M., Ma, C.-P., & Quataert, E. 2008, *Monthly Notices of the Royal Astronomical Society*, 383, 93
 Brodwin, M., Stanford, S., Gonzalez, A. H., et al. 2013, *The Astrophysical Journal*, 779, 138
 Bruzual, G. & Charlot, S. 2003, *Monthly Notices of the Royal Astronomical Society*, 344, 1000
 Bufanda, E., Hollowood, D., Jeltema, T. E., et al. 2017, *Monthly Notices of the Royal Astronomical Society*, 465, 2531
 Calzetti, D., Armus, L., Bohlin, R. C., et al. 2000, *The Astrophysical Journal*, 533, 682
 Cash, W. 1979, *The Astrophysical Journal*, 228, 939
 Conselice, C. J. 2014, *Annual Review of Astronomy and Astrophysics*, 52, 291
 Davies, R., Berbel, A., Wierorrek, E., et al. 2013, *Astronomy and Astrophysics*, 558
 Davies, R., Förster Schreiber, N., Cresci, G., et al. 2011, *The Astrophysical Journal*, 741, 69
 De Lucia, G. & Blaizot, J. 2007, *Monthly Notices of the Royal Astronomical Society*, 375, 2
 Duras, F., Bongiorno, A., Ricci, F., et al. 2020, *Astronomy and Astrophysics*
 Ellingson, E. & Yee, H. K. C. 1993, in *Evolution of Galaxies and their Environment*, ed. J. Shull & H. Thronson, 309–310
 Fassbender, R., Nastasi, A., Böhringer, H., et al. 2011, *Astronomy and Astrophysics*, 527, L10
 Fassbender, R., Nastasi, A., Santos, J. S., et al. 2014, *Astronomy and Astrophysics*, 568
 Fontana, A., D'Odorico, S., Poli, F., et al. 2000, *The Astronomical Journal*, 120, 2206
 Galametz, M., Madden, S., Galliano, F., et al. 2009, *Astronomy and Astrophysics*, 508, 645
 Greene, J. E. & Ho, L. C. 2005, *The Astrophysical Journal*, 630, 122
 Gunn, J. E. & Gott J. Richard, I. I. 1972, *The Astrophysical Journal*, 176, 1
 Harrison, E. 1974, *The Astrophysical Journal Letters*, 191, L51
 HI4PI Collaboration, Ben Bekhti, N., Flöer, L., et al. 2016, *Astronomy and Astrophysics*, 594, A116
 Hilton, M., Lloyd-Davies, E., Stanford, S. A., et al. 2010, *The Astrophysical Journal*, 718, 133
 Hippelein, H., Meisenheimer, K., & Roeser, H. 1996, *Astronomy and Astrophysics*, 316, 29
 Hopkins, P. F., Hernquist, L., Cox, T. J., et al. 2006, *The Astrophysical Journal Supplement Series*, 163, 1

- Husemann, B., Bennert, V. N., Jahnke, K., et al. 2019, *The Astrophysical Journal*, 879, 75
- Krawczyk, C. M., Richards, G. T., Mehta, S. S., et al. 2013, *The Astrophysical Journal Supplement Series*, 206, 4
- Kuiper, E., Hatch, N., Miley, G., et al. 2011, *Monthly Notices of the Royal Astronomical Society*, 415, 2245
- López-Sanjuan, C., Le Fèvre, O., de Ravel, L., et al. 2011, *Astronomy and Astrophysics*, 530, A20
- López-Sanjuan, C., Le Fèvre, O., Ilbert, O., et al. 2012, *Astronomy and Astrophysics*, 548, A7
- Madau, P. & Dickinson, M. 2014, *Annual Review of Astronomy and Astrophysics*, 52, 415
- Marchesi, S., Gilli, R., Lanzuisi, G., et al. 2020, *Astronomy and Astrophysics*, 642, A184
- Martini, P., Miller, E., Brodwin, M., et al. 2013, *The Astrophysical Journal*, 768, 1
- Martini, P., Sivakoff, G. R., & Mulchaey, J. S. 2009, *The Astrophysical Journal*, 701, 66
- McCarthy, I., Frenk, C., Font, A., et al. 2008, *Monthly Notices of the Royal Astronomical Society*, 383, 593
- McGaugh, S. S. & Schombert, J. M. 2014, *The Astronomical Journal*, 148, 77
- Menanteau, F., González, J., Juin, J.-B., et al. 2010, *The Astrophysical Journal*, 723, 1523
- Merlin, E., Pilo, S., Fontana, A., et al. 2019, *Astronomy and Astrophysics*, 622
- Miley, G. K., Overzier, R. A., Zirm, A. W., et al. 2006, *The Astrophysical Journal Letters*, 650, L29
- Moore, B., Katz, N., Lake, G., Dressler, A., & Oemler, A. 1996, *Nature Astronomy*, 379, 613
- Mushotzky, R. & AXIS Team. 2019, in *LPI Contributions*, Vol. 2135, *The Space Astrophysics Landscape for the 2020s and Beyond*, ed. Moores J.-E., King P.-L., Smith C.-L., Martinez G.-M., Newman C.-E., Guzewich S.-D., Meslin P.-Y., Webster C.-R., Mahaffy P.-R., Atreya S.-K., & Schuerger A.-C., 5025
- Narayanan, D., Dey, A., Hayward, C. C., et al. 2010, *Monthly Notices of the Royal Astronomical Society*, 407, 1701
- Park, C. & Hwang, H. S. 2009, *The Astrophysical Journal*, 699, 1595
- Patton, D., Pritchet, C., Carlberg, R., et al. 2002, *The Astrophysical Journal*, 565, 208
- Pentericci, L., Roettgering, H., Miley, G., Carilli, C., & McCarthy, P. 1997, *Astronomy and Astrophysics*, 326, 580
- Pimblet, K., Shabala, S., Haines, C., Fraser-McKelvie, A., & Floyd, D. 2013, *Monthly Notices of the Royal Astronomical Society*, 429, 1827
- Roettgering, H., Lacy, M., Miley, G., Chambers, K., & Saunders, R. 1994, *Astronomy and Astrophysics Supplement Series*, 108, 79
- Saccheo, I., Bongiorno, A., & Piconcelli, E. 2022, *Astronomy and Astrophysics* submitted
- Salpeter, E. E. 1955, *The Astrophysical Journal*, 121, 161
- Sanders, D., Soifer, B., Elias, J., et al. 1988, *The Astrophysical Journal*, 325, 74
- Santos, J., Altieri, B., Valtchanov, I., et al. 2014, *Monthly Notices of the Royal Astronomical Society*, 447
- Santos, J. S., Altieri, B., Valtchanov, I., et al. 2015, *Monthly Notices of the Royal Astronomical Society: Letters*, 447, L65
- Santos, J. S., Fassbender, R., Nastasi, A., et al. 2011, *Astronomy and Astrophysics*, 531, L15
- Tadaki, K.-i., Kodama, T., Ota, K., et al. 2012, *Monthly Notices of the Royal Astronomical Society*, 423, 2617
- The Lynx Team. 2018, *arXiv e-prints*, arXiv:1809.09642
- Tozzi, P., Santos, J., Jee, J., et al. 2014, *The Astrophysical Journal*, 799
- Travascio, A., Bongiorno, A., Tozzi, P., et al. 2020, *Monthly Notices of the Royal Astronomical Society*, 498
- van den Bosch, F. C., Aquino, D., Yang, X., et al. 2008, *Monthly Notices of the Royal Astronomical Society*, 387, 79
- Vijayaraghavan, R. & Ricker, P. 2013, *Monthly Notices of the Royal Astronomical Society*, 435, 2713
- Villalobos, A., De, L. G., Weinmann, S., Borgani, S., & Murante, G. 2013, *Monthly Notices of the Royal Astronomical Society*, 433, L49
- White, S. & Rees, M. 1978, *Monthly Notices of the Royal Astronomical Society*, 183, 341
- Williamson, R., Benson, B., High, F., et al. 2011, *The Astrophysical Journal*, 738, 139
- Wilson, G., Muzzin, A., Lacy, M., et al. 2006, *arXiv e-prints*, astro